ChemElectroChem

Research Article
doi.org/10.1002/celc.202500335

Chemistry Europe
European Chemical Societies Publishing

www.chemelectrochem.org

Simple Fabrication Method of Needle-Type Carbon-Disk Microelectrodes Using Conductive Thermoplastics

Luiz F. Z. Felipe and Gabriel N. Meloni*

Carbon-based microelectrodes are extensively used for sensing applications and space-resolved electrochemistry experiments like scanning electrochemical microscopy (SECM). For the later, needle-type disk microelectrodes, having a thin layer of insulator around the conductive disk, are of great interest due to their mass transport characteristics and small dimensions, allowing them to be brought to close proximity of the substrate. Existing fabrication methods for carbon microelectrodes use carbon fibers or the deposition of pyrolytic carbon, which can limit the possible radii of the fabricated microelectrodes and reproducibility. A simple method is presented for fabricating needle-type carbon-disk microelectrodes using conductive thermoplastic filaments that are usually employed for 3D printing. Using the heat of a candle to melt the thermoplastic inside micro and nanopipettes, microelectrodes with radii smaller than 30 µm are fabricated. Through experiments, the electrodic surface is revealed to be partially blocked, with a complex relation between the size and interspacing of the conductive sites. Simulations clarify the surface properties and demonstrate the suitability of these electrodes for SECM. As a proof-of-concept, the carbon surface is evaluated for sensing, showing that the low capacitance of the electrodes and carbon surface can be used for dopamine sensing and voltammetric pH measurements.

1. Introduction

Microelectrodes are extensively used in electrochemistry owing to their small physical dimensions and resulting fast mass transport rates.[1,2] Their small size allows experiments to be performed in small volumes, driving their application in biological samples,[2,3] including single-cell analyses.[4] The fast mass transport driven by radial diffusion and their small physical dimensions set microelectrodes as the perfect tool for probing gradients of concentrations over a wide range of different samples, including larger electrodes, leading to the invention of the scanning electrochemical microscope (SECM).[5–7] The ability to record spatially resolved electrochemical information, either by means of an SECM setup or by performing experiments in confined spaces, leads to the use of microelectrodes in the investigation of several complex electrochemical systems, including biological[8–10] and abiotic, in the form of local catalytic activity studies.[7,8,11]

Like conventional-sized electrodes, microelectrodes can be fabricated from a plethora of conductive materials, with platinum, gold, and carbon being the most common. Carbon-based microelectrodes have been used since the early 1980s, with a focus on investigating biological systems, especially measuring neurotransmitters, with dopamine (DA), serotonin, and norepinephrine being the most common ones.[12] The oxygen-containing functional groups on carbon surfaces are attributed to favor the adsorption of organic molecules and allow for fast electron transfer kinetics for neurotransmitters.[1,13] Carbon-based microelectrodes are also regarded as biocompatible and present low specific capacitance,[1,13,14] decreasing limits of quantification and detection, highly desirable for investigating molecules in complex environments and at small concentrations, like in biological systems.[15] Beyond the facile adsorption of organic molecules, the surface chemistry of carbon electrodes can also be explored for selective sensing of target molecules, such as the measurement of local pH using the redox cycling of surface-bound quinones.[16]

Despite the advantages, the fabrication of microelectrodes can be time-consuming and yield low reproducibility. Amongst other reasons (specifically biofouling), the low reproducibility is the reason that carbon microelectrodes used for neurochemical sensing employ liquid electrical contact,[17] allowing for quick change of electrode in a setup. The fabrication of platinum and gold microelectrodes is well documented and reproducible, consisting of a few steps, and can generate micro and even nanoelectrodes with different radii.[7,9,12,18–20] The fabrication of carbon microelectrodes generally relies on one of two approaches: a simple and easy encapsulation of carbon fiber filaments into a nonconductive material like epoxy resin,[21] or the deposition of pyrolytic carbon inside a glass nano or micropipette.[4] The first approach is more "artisanal", less systematic, and limits the electrode radius to the size of available carbon fibers. The second approach allows for the fabrication of electrodes with different radii, down to the nanometer range, but yields very low reproducibility, unless a bespoke machine is used.[22] Another advantage of the second approach in relation to the first is that

L. F. Z. Felipe, G. N. Meloni
Instituto de Química—Departamento de Química Fundamental
Instituto de Química
Universidade de São Paulo
São Paulo, SP 05508–000, Brazil
E-mail: gabriel.meloni@iq.usp.br

Supporting information for this article is available on the WWW under https://doi.org/10.1002/celc.202500335

microelectrodes with a small insulating layer around the carbon material (small RG—radius of glass[23]) can be produced, known as "needle-type disk electrodes",[24] which are of interest for space-resolved applications, including SECM.

For conventionally sized carbon electrodes, new fabrication methods have emerged, including the use of 3D printing with conductive thermoplastic filaments,[25] allowing for easy and automated fabrication of electrodes. Although conductive, these thermoplastic filaments are not as conductive as metals, and large 3D printed electrodes severely suffer from ohmic drop losses.[26] This is not an issue for microelectrodes due to the small faradaic currents recorded, and these thermoplastics are great candidates for microelectrode fabrication. In fact, Patel's research group has recently demonstrated how conductive thermoplastics and 3D printing can be used to fabricate microelectrodes and how they can be used for monitoring serotonin in biological media.[27] Due to the current spatial resolution of 3D printing technology, microelectrode sizes were limited to 100s of μm in diameter, still appropriate for several applications and, most importantly, provided a framework for developing new microelectrode fabrication methods. Here, we demonstrate a new fabrication protocol for producing needle-type carbon-disk microelectrodes that combines the simplicity of the "artisanal" fabrication methods with the capability to produce electrodes with very small RG and with varying radii, found on more complex fabrication protocols. For such, we resort to electrically conductive, carbon-containing, thermoplastic polymers to fill glass pulled micro and nanopipettes instead of carbon fibers or pyrolytic carbon. Our method is simple and quick, yielding carbon electrodes from a few micrometers to 100s nanometers in radius and RG as small as 1.4, making them useful for space-resolved electrochemistry such as local sensors and SECM probes. We explore the carbon surface of the electrodes with common, proof-of-concept applications for carbon electrodes, such as the oxidation of DA and voltammetric pH sensing using the redox cycling of surface quinones.

2. Experimental Section

2.1. Materials and Chemicals

All reagents were of analytical grade and used without further purification. Hexaammineruthenium chloride ($[Ru(NH_3)_6]Cl_3$), potassium chloride (KCl), dopamine (DA), sodium hydroxide (NaOH), and phosphate buffer saline (PBS—NaCl 0.01 M and KCl 0.01 M, pH 7.4) were purchased from Sigma–Aldrich. Phosphoric acid (H_3PO_4). was obtained from Vetec Química Fina Ltda., acetic acid (CH_3COOH) from Merck, and boric acid (H_3BO_3) from Química Brasileira to prepare 0.04 M Britton–Robinson (BR) buffer solutions. Deionized water (resistivity: 18.3 MΩ cm^{-1} at 25 °C) was used throughout. DA stock solutions (100 mM) were made in 0.01 M PBS, stored in a refrigerator, and diluted to 30 μM daily. Quartz capillary tubes, with an i.d. of 0.5 mm; o.d. of 1.2 mm, were acquired from Sutter Instrument. Polylactic acid conductive thermoplastic filament containing carbon black (CB/PLA) was purchased from Protopasta. A commercial reference electrode (Ag/AgCl, KCl 3 M from Metrohm) was used for most of the experiments, both as a reference and counter electrode, except for SECM approach curves, where an Ag/AgCl quasireference counter electrode was used. A boron-doped diamond electrode (oxygen-terminated, 1 mm in radius) was used to benchmark the fabricated electrodes' solvent window.

2.2. Electrochemical Measurements

Cyclic voltammetry and square wave voltammetry (SWV) experiments were performed inside a Faraday cage and conducted using a PGSTAT 302N potentiostat from Metrohm. The parameters for the SWV were: step potential of −0.001 V, amplitude of +0.05 V, and frequency of 45 Hz within a potential window ranging from +0.6 to −0.6 V. SECM approach curves were measured inside a Faraday cage in a custom scanning probe microscopy (SPM) rig using a 7856R FPGA card from National Instruments controlled by the WECSPM software provided by the Warwick Electrochemistry and Interfaces group.[28] Current was recorded with a DLPCA-200 transimpedance amplifier from FEMTO. Data was collected every 4 μs and averaged 256 times, giving a data acquisition rate of 1028 μs ($4 \times (256 + 1)$).

2.3. Microscopy Measurements

Optical images from the microelectrodes were recorded using an OpenFrame from Cairn, using a x40 Olympus lens with NA 0.75, using a Cairn CellCam. The microscope was part of the SPM rig. Scanning electron microscopy (SEM) images were acquired using a JSM-7401F FESEM from JEOL.

2.4. Numerical Simulations

Numerical simulations of SECM approach curves and voltammograms for selected electrodes were performed in COMSOL Multiphysics v6.2, using the transport of diluted species module with the simulation domain geometry based on the real electrode geometry as derived by microscopy images. Details of the simulation can be found in S1.

2.5. Microelectrode Fabrication

For fabricating the microelectrodes, first quartz capillaries (0.5 mm i.d. and 1.2 mm o.d.) were pulled to a sharp tip using a P-2000 Puller from Sutter, creating two equal (micro/nano) pipettes. The pulling parameters for the quartz pipettes can be found in (Section S2, Supporting Information). Two different pulling programs, resulting in 2 different pipette sizes[29] were used to see if the pipette size translated to the final electrode size. Due to the need to polish the electrodes, their radii were dictated by the polishing step, and not the original pipette opening size.

With the help of a 3D printing pen, thin strands of the CB/PLA conductive filament were fabricated (thickness < 0.5 mm) to be

inserted into the back of the pulled pipettes. The strands were generated by extruding the filament over a plastic surface, followed by extruding the filament in air, pulling the 3D pen away from the surface. If the pen was pulled faster than the extrusion speed of the pen, the filament was stretched, causing it to thin down. The thinning process can be seen in (Movie S1, Supporting Information). Thinned strands with ≈1 cm in length were inserted in the back of the micro/nanopipettes and pushed to the pipette tip using a 0.35 mm diameter copper wire, which served as an electrical connection (**Figure 1**A). The tip of the pipettes with the CB/PLA filament was placed over the flame of a candle to melt the filament strand, which can be pushed with the copper wire, forcing the material to the pipette tip. The copper wire also bonds with the melted filament, forming the electrical contact between the copper wire and the filament, without the need for any additional step for making the electrical contact. A scheme of the fabrication process of the electrodes is shown in Figure 1A, alongside a picture of a fabricated electrode (Figure 1B). The filling procedure with the candle can be seen in (Movie S2, Supporting Information), in real time, taking just a few seconds per electrode.

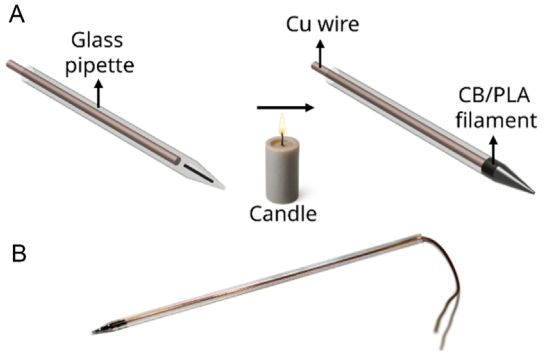

Figure 1. A) Scheme of the fabrication process of the CB/PLA conductive filament microelectrode and B) a photo of one microelectrode.

3. Results and Discussion

3.1. Voltammetric Response of the Electrodes

After the fabrication step, with the help of an affordable USB microscope, microelectrodes were inspected. Due to the "artisanal" nature of the fabrication process, several electrodes had partially filled tips with the CB/PLA material and were discarded. The success rate, like other carbon microelectrode fabrication methods,[1,13] is dependent on the training of the person fabricating the electrode, and hence cannot be meaningfully reported, but in our experience was below 50% for all users who attempted the fabrication method. Despite this, we believe that the simple and quick nature of our method, when compared to others, outweighs the low success rate, which, in our own experience, is similar to other reported methods.[14,30,31]

Electrodes that by visual inspection had a filled tip were tested by cyclic voltammetry, recorded with a scan rate of 50 mV s^{-1} in a 1 mM $[Ru(NH_3)_6]^{3+}$ in 0.1 M KCl solution. If the electrode had no electrochemical response, it was polished (30 s with a 1200-grit sandpaper) using a custom-built polishing machine[32] until a voltammetric response was seen. **Figure 2**A shows the recorded voltammograms of 5 microelectrodes with different radii (different limiting currents), where the characteristic sigmoid shape of a microelectrode voltammogram is observed.[12,33,34] Microelectrode 1 from Figure 2 is the only one of this batch that presented a voltammetric response without polishing, having a radius of ≈350 nm (measured by SEM, vide infra), roughly double that of the original pipette used (Section S2, Table S4, Supporting Information). The polishing step had two consequences: first, it created a flat disk geometry at the electrode tip, as seen in the optical microscope images (Figure 2B), and second, due to the conical shape of the pipette tip, it increased the electrode radius, resulting in the different steady-state current values seen in Figure 2A.

From the steady-state currents (i_{ss}) of the voltammograms in Figure 2, and with knowledge of the electrode RG, derived from the SEM images (**Figure 3** and S4, Supporting Information), the radius (*a*) of each electrode can be calculated using Equation (1),[23] where *X* is an RG dependent constant, *C* is the redox probe

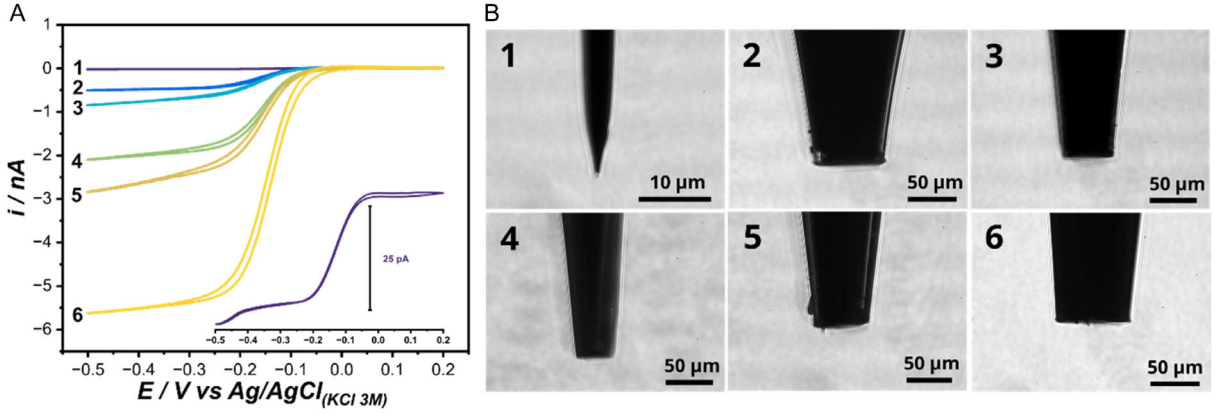

Figure 2. A) Cyclic voltammograms recorded in 0.1 M KCl containing 1 mM $[Ru(NH_3)_6]^{3+}$ solution with different microelectrodes (1–6) and B) their respective microscope images. Scan rate: 50 mV s^{-1}.

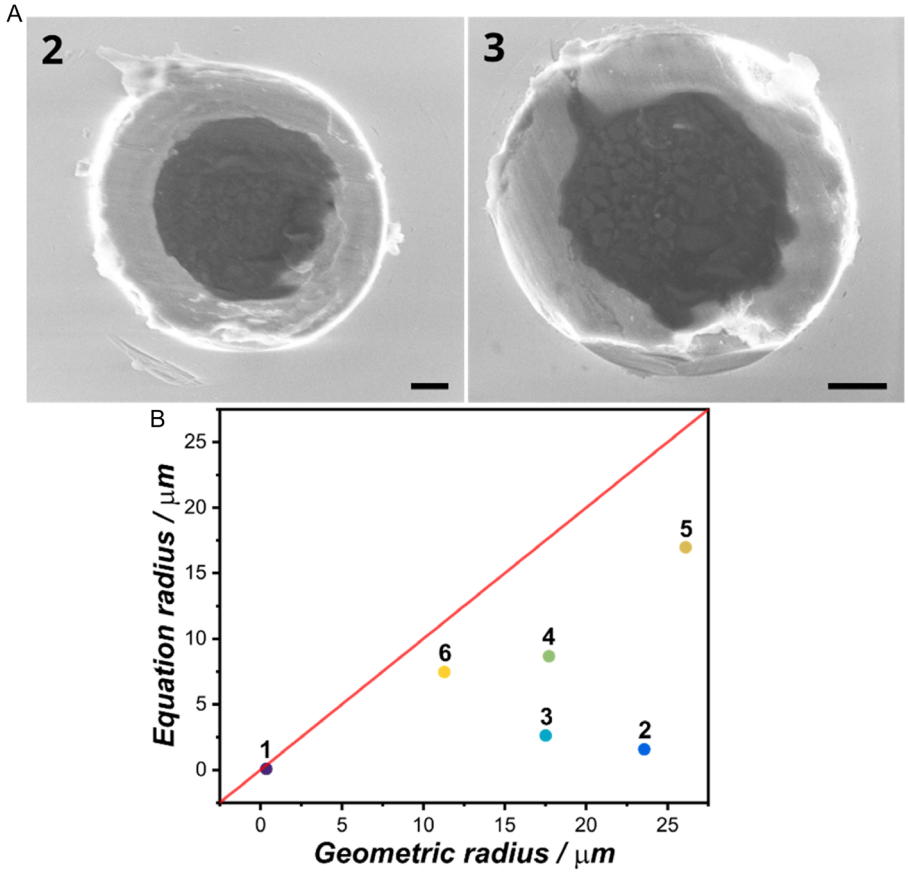

Figure 3. A) SEM images (scale bar: 20 μm) of microelectrodes 2 and 3 from Figure 2 and B) relation between the radii found by Equation (1) and the geometric radii obtained from the SEM images. Microelectrode number and dot color are the same as in Figure 2, panel A.

concentration (1 mM), F is Faraday's constant and D the diffusion coefficient of the redox probe used (6.5×10^{-6}cm^2 s^{-1} for $[Ru(NH_3)_6]^{+3/+2}$).[35]

$$i_{ss} = XnFDCa \quad (1)$$

The RG of all electrodes was between 1.4 and 1.6 (Table S5, Supporting Information), and back-diffusion will contribute to mass transport toward the electrode surface, a characteristic of needle-type microelectrodes. To account for that, the multiplier constant (X) in Equation (1), usually taken as 4 for electrodes with RG equal to or larger than 10, is increased according to the RG value, as proposed by Zoski et al.[23] The radius of each microelectrode can also be derived from the SEM images, as shown in Figure 3 for electrodes 2 and 3 from Figure 2. It should be noted that most of the voltammograms in Figure 2 do not have a true steady-state current, as we will delve further, and, for calculating the radius using Equation (1), the largest cathodic current value was used. Although this is not strictly rigorous, it shows the difference between the calculated radii and what is recovered from SEM images, which is summarized in Figure 3B. The radii of all electrodes in Figure 3B, geometric and calculated, can be found in (Table S5, Supporting Information). Equation (1) severely underestimates the radii, suggesting the overall electrochemical response of the fabricated microelectrodes is that of a smaller disk microelectrode. The same phenomenon was reported by Patel,[27] where all the 3D printed microelectrodes fabricated, using the same conductive thermoplastic filament we employ here, had a smaller radius derived from Equation (1) than from SEM images. What is reasoned by Patel is that the surface is only partially conductive owing to the distribution of conductive carbon sites on the polymeric matrix of the thermoplastic, which behaves as a partially blocked surface,[36] or a spatially heterogeneous electrode.[37]

Understanding this behavior is complicated, and although Compton and coworkers have laid the groundwork for mathematical modeling of it, it still requires some assumptions to be made regarding the size and spacing of the electroactive sites.[37] To better understand the behavior of our microelectrodes, we focus on electrodes 2 and 3 from Figure 2 (also shown in Figure 3A), which have geometric radii of 23.6 and 17.5 μm and calculated radii of 1.6 and 2.6 μm, respectively. First, we compare the experimental currents with simulated ones, using the geometry derived from SEM and optical microscopy (**Figure 4**). For the simulations, fast electron transfer rate ($k_0 = 1$ cm s^{-1}) is assumed, which is reasonable to assume for hexamine ruthenium over carbon.[38–40] The voltammetric profile is very different between experiments and simulations, with experimental ones (Figure 4—black dots) showing much smaller currents, low

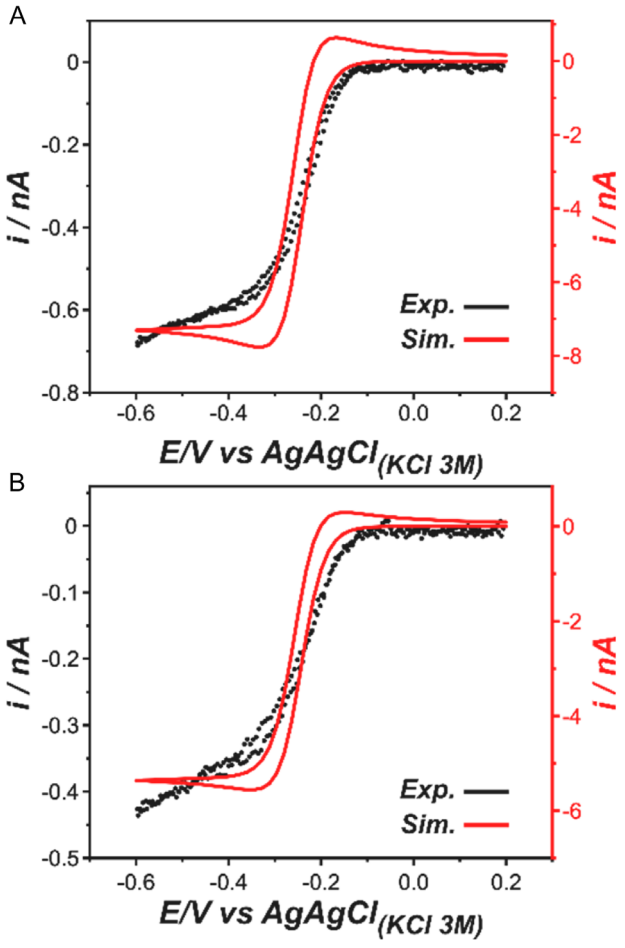

Figure 4. Experimental (dots) and simulated (red trace) cyclic voltammograms recorded with microelectrodes A) 2 and B) 3 from Figure 2 and 3. Experimental voltammograms were recorded in a 1 mM $[Ru(NH_3)_6]^{3+}$ in 0.1 M KCl solution. Scan rate 50 mV s^{-1}. Simulated voltammograms use the same experimental framework and the electrode geometry derived from optical and electron microscopies (Figure 2 and 3).

hysteresis, and the absence of a true steady-state current. Simulations (Figure 4—red trace) predict a much larger current and large hysteresis, pointing to the contribution of linear diffusion to the overall mass transport, owing to the large electrode size.

These suggest that only part of the surface is electroactive and that the size of electroactive sites and space between them is such that, at the experimental conditions (scan rate of 50 mV s^{-1}), there is no complete overlap of the diffusion layers of the active sites, the limiting case described by Amatore,[36] else the simulated and experimental voltammetric profile would match. For larger electrodes, even if a complete overlap of the diffusion layer is seen, the voltammetric profile would be that of a slower electron transfer rate, with an apparent rate constant of $(\theta - 1)k_0$, where theta is the percentage of the electrode area blocked/not active.[36] This is only true if mass transport is only by linear diffusion, which is clearly not the case here.[37] Slower rate constants in microelectrodes manifest as a decrease in the slope on the linear region of the sigmoid voltammogram, seen by the difference in quartile-potentials,[41] despite the lack of a true steady-state currents, we can estimate, at least to a first order, the rate constant from the experimental voltammograms using Mirkin's simple analyses method (Figure S5, Supporting Information).[41] The calculated rate constants for both microelectrodes are ≈0.021 cm s^{-1}, smaller than what is expected for mass-transport limited voltammograms of electrodes with the geometric and calculated radii of electrodes 2 and 3 (see Section S4, Supporting Information). This points to a surface that is partially blocked and to the complicated (or at least unknown) interspacing and size relation of the carbon sites on the surface. Not only is there no complete diffusion layer overlap from the active sites, as seen above, but now it is also clear that the sites are not independent, as the derived rate constant is smaller than expected. If they were all independent, behaving as an array of microelectrodes, the derived rate constants should match that of mass-transport limited voltammograms.

To better understand the surface coverage, we can look at the mean diffusional length during the experiment, which can be approximated by Einstein's Equation (Equation (2)). Where $\langle x \rangle$ is the mean square displacement of a particle (mean diffusional length), D is the diffusion coefficient, and t is the time, which can be extracted from the experimental voltammograms. To recover this value, we take the difference between the maximum value of the first derivative of the current over time and the time when the derivative starts to increase from zero (Figure S6, Supporting Information) and take it as the "time to steady-state", when the concentration gradient stops growing. The values were calculated as 2.0 s for microelectrode 2 and 2.8 s for microelectrode 3. This is an approximation, and other expressions do exist to calculate the same time parameter or the diffusion layer length over microelectrodes, but they assume the surface is uniformly active. Also, this approach will overestimate the diffusional length as it is not the time at which the diffusion layer stops growing, but the time the concentration gradient stops changing. For microelectrode 2 (Figure 2 and 4A), the diffusional length is 51 µm, and for microelectrode 3 (Figure 2 and 4B), 60 µm. As we deduced that the active sites are neither independent nor completely connected, this diffusion length gives a sense of the order of magnitude of the interspacing between the sites, as a smaller interspacing than this could result in heavily overlapping diffusion layers, while a larger interspacing in individual diffusion layers at each site.[37]

$$\langle x \rangle = \sqrt{2Dt} \tag{2}$$

We reason that this complex interplay between the diffusion layers explains the lack of a true steady-state current, seen in Figure 4. The electrode geometry (Figure 3) is that of a flat disk, with no marked surface features (porosity, cavities, etc.) that could possibly explain the lack of steady-state current. This is likely a result of a mix of linear and radial diffusion over the electrode surface different conductive sites, different sizes of these sites, and different interspacing between them. The overall contribution of linear and radial diffusion is, most likely, changing over time, with the diffusion layer of some of these sites growing over time, and overlapping with each other, resulting in an ever-growing apparent electrode surface over the potential excursion. The issue of not knowing the size of the conductive sites and

their interspacing has been tackled in the literature concerning 3D printed electrodes. Patel's and O'Neil's groups have been investigating the particle size and size distribution, finding conductive particle clusters ranging from hundreds of nanometers to 250 µm in size.[42] Interestingly, most reports of large 3D printed electrodes show an area that behaves as if it is 100% active, a large contrast to what is seen in the microscale. This discrepancy between the length scales, to our reasoning, points to the heterogeneous nature of the conductive sites' size and interspacing.

3.2. SECM Approach Curves

One main application of microelectrodes, and in particular needle-type microelectrodes, is in scanning probe techniques like SECM, where they are used to probe concentration gradients around substrates. Needle-type microelectrodes are of interest as the small RG value allows for larger currents to be recorded, due to back diffusion, and the electrode to be physically positioned closer to surfaces being investigated, in both cases increasing experimental sensitivity, very desirable for investigating small concentration gradients, such as the ones seen in biological samples.[15] To explore this ability in our microelectrodes, SECM approach curves over glass substrates were performed with microelectrodes 2 and 3 using a 1 mM $[Ru(NH_3)_6]^{3+}$ in 1 M KCl solution, with the working electrode biased at −0.6 V and at an approach rate of 5 µm s^{-1}. With knowledge of the electrode geometry, fitting experimental approach curves with theory is possible with little effort,[43] but here, due to the complicated nature of the heterogeneous carbon surface of the microelectrodes, fitting the data is not straightforward. The profile of the approach curve is dependent on the electrode radius, RG, and the electrode-substrate separation. Since our electrode is partially blocked, it is not immediately clear which radius value to use, geometric or calculated.

At first, using the calculated electrode radius, derived from Equation (1) (Figure 3), seems appropriate, but then the question is which electrode body geometry to consider. Our fabricated microelectrodes have a small RG value, which favors back diffusion even if the electrode is partially blocked. As such, using the calculated microelectrode radius and the RG value derived from Figure 3 would result in an electrode that is physically much smaller, which impacts the approach curve profile and minimal approach distance. If instead we use the calculated electrode radius and the outer glass radius from SEM images to describe the geometry, the RG value would be much larger than the real one, and no back diffusion would be considered. The physical dimensions of the microelectrode greatly impact the profile of an approach curve, and the true geometry must be considered.

The key here is understanding the overall effect that a partially blocked, space-heterogeneous surface has on the microelectrode response and how this affects a hindered diffusion approach curve. The microelectrode current is proportional to the concentration gradient at the electrode/solution interface, given by $\nabla C/\delta$, where ∇C is the variation of concentration within the thickness of the diffusion layer, δ. Although for the approach curves the microelectrodes were biased at −0.6 V, which should reduce $[Ru(NH_3)_6]^{3+}$ at diffusion-limited rates, i.e., surface concentration should be near zero, this is only true at the conductive carbon sites. As the surface is partially blocked and, as we mentioned above, the size distribution and interspacing of these active sites must be heterogeneous, the average concentration over the entire electrode surface will not be zero. The diffusion layer will also be much smaller than that of a 100% active surface. Hence, the concentration gradient will be very different from that of an electrode with the same geometry and the entire surface active. To reproduce this effect in simulations, we can assume an apparent value of k_0 that would modulate the concentration gradient. This is the same approach proposed by Amatore for partially blocked electrodes (not microelectrodes),[36] where the apparent rate constant directly expresses the percentage of blockage of the surface, which, unfortunately, is not the case for microelectrodes (vide supra). To find suitable values of an apparent k_0, simulations of the microelectrodes in bulk solution biased at −0.6 V to reduce $[Ru(NH_3)_6]^{3+}$ were performed using the microelectrode's real geometry, derived from Figure 2 and 3, and varying the values of k_0 until the simulated current matched that at the start of the experimental approach curves. This resulted in values of 7×10^{-7} cm s^{-1} and 6.6×10^{-7} cm s^{-1} for microelectrodes 2 and 3, respectively.

These values were used to simulate hindered diffusion approach curves for both microelectrodes. The experimental normalized approach curves, together with simulated ones, can be seen in **Figure 5**, where the expected decrease in normalized current with decrease in normalized electrode/substrate separation (d/a) for hindered diffusion is seen.[6,43]

Using the microelectrodes' real geometry and the adjusted apparent k_0 values, the simulated approach curves (Figure 5—black traces) match closely with the experimental data (Figure 5—red dots) for both microelectrodes. The advantages of the low RG value of the needle-type microelectrodes fabricated are evident when comparing the experimental curves with simulated ones using the real electrode radius, same values of apparent k_0, but with RG values of 5 (Figure 5—light blue) and 10 (Figure 5—purple trace). The experimental curves for both microelectrodes, and the simulated with the real RG values, are much sharper, with the normalized current decreasing from 1 at very small d/a values, allowing the electrode to be approached much closer to the substrate, which favors space-resolved electrochemical experiments.[44] The impact of the concentration gradient on the profile of the approach curves is evident when we compare the experimental data with simulations for the same geometry but using a k_0 value of 1 cm s^{-1} (Figure 5—green dashed trace). Under this condition, the normalized current decreases from 1 at much larger d/a values, showing that the substrate hinders diffusion toward the microelectrode even at much larger distances. These results from a much larger concentration gradient developed at the electrode/solution interface at this large rate constant (Figure S2A, Supporting Information). A smaller concentration gradient could also be simulated by considering a fast rate constant and using the calculated electrode radius and the outer electrode body dimensions derived from electron microscopy. With this approach, the resulting simulated approach curves,

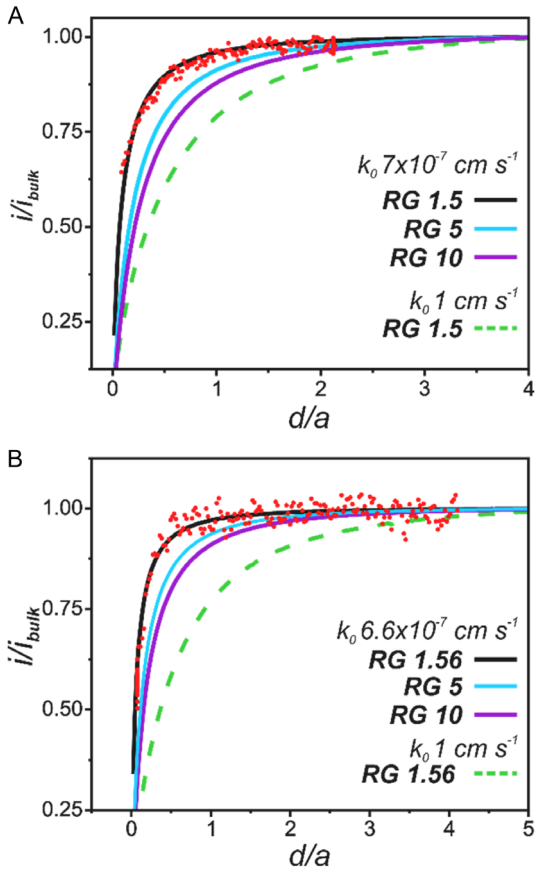

Figure 5. Experimental (dots) and simulated (traces) SECM approach curves toward an insulator substrate (glass) with microelectrodes A) 2 and B) 3 in Figure 2 and 3. Experimental approach curves recorded in a 1 mM $[Ru(NH_3)_6]^{3+}$ in 0.1 M KCl solution with the microelectrode biased at −0.6 V. Approach rate was fixed at 5 µm s^{-1}. Simulations performed at the same experimental conditions using the real microelectrode radius and varying k_0 and RG values, described within the Figure. Simulations portrayed by the solid black traces are the best fit for the experimental data.

when compared with the approach curves in Figure 5 (black traces), are similar but show different current/distance behaviors when the electrode is near the substrate (Figure S2B, Supporting Information). This highlights the importance of understanding what limits the electrode response, the concentration gradient. Although both alternatives to simulating the concentration gradient result in similar curves, we believe that our proposed approach better represents the real experimental concentration gradient and the electrode's current/distance response. Despite the complicated heterogeneous nature of the surface of the microelectrodes, it is still possible to characterize their electrochemical performance, as we have explored for cyclic voltammetry and now, the SECM approach curves.

3.3. Exploring the Carbon Surface

3.3.1. pH Sensor

The conductive sites at the surface of the microelectrodes are made of carbon black, and as such, the surface chemistry of carbon can be explored for chemical sensing. Oxides on the carbon surfaces, like quinones,[1,45] undergo a proton-coupled electron transfer reaction and can be used as a voltammetric pH sensor by monitoring the pH-dependent potential shift of the surface-bound quinones reduction.[16,20,46] This has already been demonstrated for 3D printed electrodes using similar conductive thermoplastics as the one used here,[47] but there is still a question whether this type of electrode could be miniaturized, since it is a voltammetric sensor, the signal depends on the quinone coverage at the surface, and the distribution/packing of these quinones at the surface. Microelectrodes were functionalized to promote the formation of stable surface-bound quinones, using a protocol reported in the literature, exploring anodization in H_2SO_4 solution.[46,47] To investigate whether the microelectrodes' surfaces would behave similarly to other carbon-based electrodes and respond to pH changes, we use square wave voltammetry to measure the reduction of the surface-bound quinones in 0.04 M BR buffer solutions with different pHs. **Figure 6**A shows the resulting voltammograms for microelectrode 4 in Figure 2 (SEM image can be seen in Figure S4, Supporting Information). A plot of the reduction peak potential position (E) as a function of the pH can be seen in Figure 6B, where a linear response to pH change ($E = 0.4258 - 0.0684\text{pH} - R^2 = 0.991$), with a near-Nernstian slope, is seen, as expected for this type of electrode.[47] Four other microelectrodes were also functionalized, resulting in a similar linear response of peak potential position with pH (Section S6, Figure S7, Supporting Information). Considering all sensors, we find an average gradient of—67.3 ± 0.7 mV pH^{-1} ($n = 5$). It should be noted that the electrode's polymeric matrix, PLA, can react in very alkaline medium, by either hydrolysis or saponification, which is widely used as a surface treatment to improve the electrochemical performance of 3D printed electrodes.[48,49] As such, the stability of these pH sensors might be limited in alkaline medium. At the pH range used here, like what has been reported elsewhere,[47] we have not seen degradation of the signal even at the most alkaline solution. All experiments were performed in an aerated solution, and even so, oxygen reduction interference is small, being most pronounced at the highest pH solution. As quinones are known to catalyze oxygen reduction, we reason that the partially blocked electrode surface favors low quinone coverage, which has been reported as a strategy to avoid oxygen reduction interference.[46,47]

3.3.2. Dopamine Detection

Carbon-based microelectrodes are often used for neurotransmitter electrochemical sensing, primarily DA and focusing on in vivo analysis,[45,50] owing to their surface chemistry with oxygen-containing groups.[1,13] To assess if the fabricated microelectrodes could be employed for DA sensing, whose needle-type geometry will be favorable for space-resolved and in vivo experiments, cyclic voltammograms were recorded in 0.01 M PBS solution containing 30 µM DA at varying scan rates (0.5, 1, and 5 V s^{-1}) using microelectrode 4 from Figure 2. The resulting voltammograms can be seen in Figure 6C, where the oxidation process of DA can be seen for all

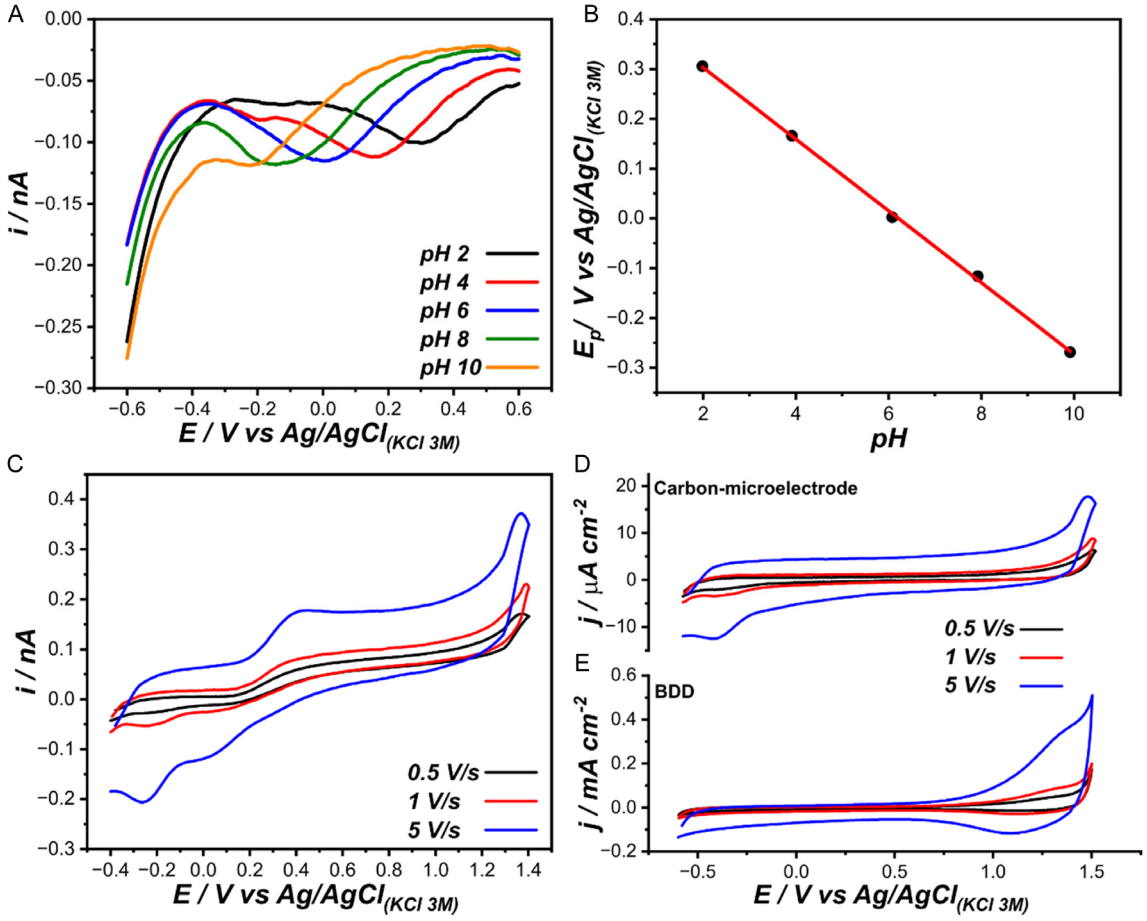

Figure 6. A) Square wave voltammograms recorded using the functionalized microelectrode 4 (Figure 2) in 0.04 M BR solutions with different pH values (2, 4, 6, 8, and 10) and B) linear fit between the reduction peak current potential and pH. C) Cyclic voltammograms recorded using the same electrode (microelectrode 4) in a 0.01 M PBS solution with 30 μM DA at different scan rates (0.5, 1, and 5 V s^{-1}). Cyclic voltammograms recorded in 0.01 M PBS solution using D) microelectrode 4 and E) a 2 mm diameter disk BDD electrode.

scan rates at around +0.4 V. As DA is usually sensed using fast scan cyclic voltammetry, at voltammetric scan rates of 100s of V s^{-1}, which we cannot perform due to instrumental limitations, background capacitive current is a severe limitation and electrodes with low capacitance are desirable to minimize background current. We measured the specific capacitance of our microelectrode by recording voltammograms in 0.01 M PBS solution (Figure 6D) and dividing the background current at 0 V by the scan rate and dividing this value by the geometric area of the microelectrodes, derived from SEM images (Figure S4, Supporting Information). We found a value of 0.316 ± 0.255 μF cm^{-2}. We repeated the same experiment with boron-doped diamond (BDD) electrodes, which are notorious for low specific capacitance,[51] and found values of 6.997 ± 0.332 μF cm^{-2}. Our fabricated microelectrodes exhibit a specific capacitance smaller than that of BDD electrodes, making them potential tools for fast scanning measurements and in vivo DA detection. We reason that the low specific capacitance, even lower than BDD, arises from the surface heterogeneity, as only the carbon conductive sites will contribute to the capacitance of the electrode. As we do not know the percentage of the microelectrode's area that is active, as mentioned before, we cannot report a more representative specific capacitance figure, which would be divided by the active area of the electrode. Our microelectrodes also have a wide solvent window, measured as 3.35 V in 0.01 M PBS solution, similar to BBD, measured as 3.48 V in the same solution (Section S7, Figure S8, Supporting Information), which is advantageous for a wide range of sensing and measuring applications.

4. Conclusions

We introduce a simple, low-cost route to needle-type carbon-disk micro/nanoelectrode fabrication by filling micro and nanopipettes with a conductive CB/PLA thermoplastic, used for 3D printing. Our method yields microelectrodes with a wide range of radii and small RG (as low as 1.4), making them useful for SECM experiments, enabling close approach to substrates. The electrochemical behavior of the fabricated microelectrodes highlighted the heterogeneous, partially blocked nature of the conductive thermoplastic surface, which was reasoned with the support of numerical simulations. We performed SECM approach curves over an insulating substrate, demonstrating the advantage of

needle-type electrodes for space-resolved electrochemical measurements. We also explore the carbon chemistry of the microelectrode surface via voltammetric pH sensing using the redox cycling of surface-bound quinones with near-Nernstian response. The fabricated microelectrodes have low specific capacitance and a wide solvent window (3.35 V in 0.01 M PBS), supporting their sensing application, as we demonstrate for dopamine. Our simple fabrication method is an alternative for the quick fabrication of needle-type carbon-disk microelectrodes that can be used for SECM experiments and miniaturized chemical sensing.

Acknowledgements

This research was supported by São Paulo Research Foundation (FAPESP), grant numbers: 2021/00800-3 (G.N.M.) and 2025/00970-7 (L.F.Z.F.). The present work was carried out with the support of the Institute of Chemistry and its Analytical Center—Code CAIQUSP/100. This study was financed in part by the Coordenação de Aperfeiçoamento de Pessoal de Nível Superior—Brasil (CAPES) - Finance Code 001, Program 33002010191P0.

Conflict of Interest

The authors declare no conflict of interest.

Data Availability Statement

The data that support the findings of this study are available from the corresponding author upon reasonable request.

Keywords: 3D printing · microelectrode · partially blocked surface · scanning electrochemical microscopy · scanning electrochemical probe microscopy

[1] R. L. McCreery, *Chem. Rev.* **2008**, *108*, 2646.
[2] C. Yang, E. Trikantzopoulos, M. D. Nguyen, C. B. Jacobs, Y. Wang, M. Mahjouri-Samani, I. N. Ivanov, B. J. Venton, *ACS Sens.* **2016**, *1*, 508.
[3] M. Devi, M. Vomero, E. Fuhrer, E. Castagnola, C. Gueli, S. Nimbalkar, M. Hirabayashi, S. Kassegne, T. Stieglitz, S. Sharma, *J. Neural Eng.* **2021**, *18*, 041007.
[4] C. Yang, K. Hu, D. Wang, Y. Zubi, S. T. Lee, P. Puthongkham, M. V. Mirkin, B. J. Venton, *Anal. Chem.* **2019**, *91*, 4618.
[5] A. J. Bard, F. R. F. Fan, J. Kwak, O. Lev, *Anal. Chem.* **1989**, *61*, 132.
[6] J. Kwak, A. J. Bard, *Anal. Chem.* **1989**, *61*, 1221.
[7] S. Amemiya, A. J. Bard, F.-R. F. Fan, M. V. Mirkin, P. R. Unwin, *Annu. Rev. Anal. Chem.* **2008**, *1*, 95.
[8] K. Eckhard, X. Chen, F. Turcu, W. Schuhmann, *Phys. Chem. Chem. Phys.* **2006**, *8*, 5359.
[9] L. Huang, Z. Li, Y. Lou, F. Cao, D. Zhang, X. Li, *Materials* **2018**, *11*, 1389.
[10] F. Conzuelo, A. Schulte, W. Schuhmann, *Proc. R. Soc. A* **2018**, *474*, 20180409.
[11] A. Preet, T.-E. Lin, *Catalysts* **2021**, *11*, 594.
[12] R. M. Wightman, *Anal. Chem.* **1981**, *53*, 1125A.
[13] P. Puthongkham, B. J. Venton, *Analyst* **2020**, *145*, 1087.
[14] Z. Shao, Y. Chang, B. J. Venton, *Anal. Chim. Acta* **2022**, *1223*, 340165.
[15] K. Cremin, G. N. Meloni, D. Valavanis, O. S. Soyer, P. R. Unwin, *ACS Meas. Sci. Au* **2023**, *3*, 361.
[16] Z. J. Ayres, A. J. Borrill, J. C. Newland, M. E. Newton, J. V. Macpherson, *Anal. Chem.* **2016**, *88*, 974.
[17] J. T. Cox, J. P. Guerrette, B. Zhang, *Anal. Chem.* **2012**, *84*, 8797.
[18] M. Gonsalves, A. L. Barker, J. V. Macpherson, P. R. Unwin, D. O'Hare, C. P. Winlove, *Biophys. J.* **2000**, *78*, 1578.
[19] I. Traxler, T. D. Singewald, G. Schimo-Aichhorn, S. Hild, M. Valtiner, *Corros. Rev.* **2022**, *40*, 515.
[20] N. B. Biswas, T. Read, K. J. Levey, J. V. Macpherson, *ACS Electrochem.* **2025**, *1*, 1532.
[21] A. G. Zestos, C. Yang, C. B. Jacobs, D. Hensley, B. J. Venton, *Analyst* **2015**, *140*, 7283.
[22] P. Actis, S. Tokar, J. Clausmeyer, B. Babakinejad, S. Mikhaleva, R. Cornut, Y. Takahashi, A. López Córdoba, P. Novak, A. I. Shevchuck, J. A. Dougan, S. G. Kazarian, P. V. Gorelkin, A. S. Erofeev, I. V. Yaminsky, P. R. Unwin, W. Schuhmann, D. Klenerman, D. A. Rusakov, E. V. Sviderskaya, Y. E. Korchev, *ACS Nano* **2014**, *8*, 875.
[23] C. G. Zoski, M. V. Mirkin, *Anal. Chem.* **2002**, *74*, 1986.
[24] B. B. Katemann, W. Schuhmann, *Electroanalysis* **2002**, *14*, 22.
[25] W. B. Veloso, T. R. L. C. Paixão, G. N. Meloni, *Electrochim. Acta* **2023**, *449*, 142166.
[26] W. B. Veloso, T. R. L. C. Paixão, G. N. Meloni, *Anal. Chem.* **2024**, *96*, 14315.
[27] Z. Xue, K. Patel, P. Bhatia, C. L. Miller, R. S. Shergill, B. A. Patel, *Anal. Chem.* **2024**, *96*, 12701.
[28] Warwick Electrochemical Scanning Probe Microscopy (WEC-SPM), https://warwick.ac.uk/fac/sci/chemistry/research/electrochemistry/wec-spm (accessed: August 2025).
[29] T. P. White, T. D. Wood, *Anal. Chem.* **2003**, *75*, 3660.
[30] M. L. A. V. Heien, P. E. M. Phillips, G. D. Stuber, A. T. Seipel, R. M. Wightman, *Analyst* **2003**, *128*, 1413.
[31] K. C. Morton, C. A. Morris, M. A. Derylo, R. Thakar, L. A. Baker, *Anal. Chem.* **2011**, *83*, 5447.
[32] FuNIILab custom polishing machine, https://www.funiilab.com/funiitriz (accessed: November 2025).
[33] M. A. Dayton, J. C. Brown, K. J. Stutts, R. M. Wightman, *Anal. Chem.* **1980**, *52*, 946.
[34] A. M. Bond, *Analyst* **1994**, *119*, 1R.
[35] F. Liu, G. Kolesov, B. A. Parkinson, *J. Electrochem. Soc.* **2014**, *161*, H3015.
[36] C. Amatore, J. M. Savéant, D. Tessier, *J. Electroanal. Chem. Interfacial Electrochem.* **1983**, *147*, 39.
[37] T. J. Davies, C. E. Banks, R. G. Compton, *J. Solid State Electrochem.* **2005**, *9*, 797.
[38] A. N. Patel, M. G. Collignon, M. A. OConnell, W. O. Y. Hung, K. McKelvey, J. V. MacPherson, P. R. Unwin, *J. Am. Chem. Soc.* **2012**, *134*, 20117.
[39] S. C. S. Lai, A. N. Patel, K. McKelvey, P. R. Unwin, *Angew. Chem.—Int. Ed.* **2012**, *51*, 5405.
[40] A. G. Güell, K. E. Meadows, P. V. Dudin, N. Ebejer, J. V. Macpherson, P. R. Unwin, *Nano Lett.* **2014**, *14*, 220.
[41] M. V. Mirkin, A. J. Bard, *Anal. Chem.* **1992**, *64*, 2293.
[42] S. Ahmed, E. G. Arthur, T. Obrzut, R. Shergill, A. Williams, K. Wamalwa, Z. D. Epright, C. Darvish, Y. Khatib, W. Li, B. A. Patel, G. D. O'Neil, *ACS Electrochem.* **2025**, *1*, 2386.
[43] R. Cornut, C. Lefrou, *J. Electroanal. Chem.* **2007**, *604*, 91.
[44] C. L. Bentley, J. Edmondson, G. N. Meloni, D. Perry, V. Shkirskiy, P. R. Unwin, *Anal. Chem.* **2019**, *91*, 84.
[45] M. L. Huffman, B. J. Venton, *Analyst* **2009**, *134*, 18.
[46] S. J. Cobb, Z. J. Ayres, M. E. Newton, J. V. Macpherson, *J. Am. Chem. Soc.* **2019**, *141*, 1035.
[47] F. M. Rabboh, G. D. O'Neil, *Anal. Chem.* **2020**, *92*, 14999.
[48] D. P. Rocha, R. G. Rocha, S. V. F. Castro, M. A. G. Trindade, R. A. A. Munoz, E. M. Richter, L. Angnes, *Electrochem. Sci. Adv.* **2022**, *2*, e2100136.
[49] A. Koterwa, I. Kaczmarzyk, S. Mania, M. Cieslik, R. Tylingo, T. Ossowski, R. Bogdanowicz, P. Niedziałkowski, J. Ryl, *Appl. Surf. Sci.* **2022**, *574*, 151587.
[50] C. B. Jacobs, I. N. Ivanov, M. D. Nguyen, A. G. Zestos, B. J. Venton, *Anal. Chem.* **2014**, *86*, 5721.
[51] J. V. Macpherson, *Phys. Chem. Chem. Phys.* **2015**, *17*, 2935.

Manuscript received: August 25, 2025
Revised manuscript received: November 14, 2025
Version of record online: